Turbulence Modelling and Cavitation Dynamics in Cryogenic Turbopumps

Mani, K.V.; Cervone, Angelo; Hickey, J.P.

Publication date
2016

Document Version
Accepted author manuscript

Published in
Space propulsion 2016

Turbulence Modelling and Cavitation Dynamics in Cryogenic Turbopumps

Karthik Mani[1,2], **Angelo Cervone**[1], and **Jean-Pierre Hickey**[2,3]
[1] *Aerospace Engineering, Delft University of Technology, Kluyverweg 1, Delft, 2629 HS, the Netherlands*
[2] *Spacecraft Department, German Aerospace Center (DLR), Göttingen, 37073, Germany*
[3] *Mechanical and Mechatronics Engineering, University of Waterloo, Waterloo, N2L 3G1, Canada*
Emails: karthikvenkateshmani@gmail.com ; a.cervone@tudelft.nl ; jean-pierre.hickey@uwaterloo.ca

KEYWORDS: Turbopump, cavitation, turbulence modelling, bubble dynamics, thermo-sensitive cavitation

ABSTRACT

Robust turbulence modelling of cavitating flows in cryogenic turbopump inducers are essential for accurate prediction of their performance characteristics and increased reliance on numerical simulations during their early design stages. This work focuses on (1) the sensitivities related to the choice of turbulence models on the cavitation prediction in flow setups relevant to cryogenic turbopump inducers and (2) the characterisation of cavitation bubble dynamics in flows past rotating turbopump inducers, with and without thermal effects, in an effort to characterise the potential turbulence-cavitation interaction. First, the isolation of the influence of turbulence closure models is done by abstracting three canonical problems and studying them individually to separately consider cavitation occurring in flows with a bluff body pressure drop, adverse pressure gradient, and blade passage contraction. The choice of turbulence model plays a significant role in the prediction of the phase-distribution in the flow. It was found that the sensitivity to the closure model depends on the choice of cavitation model and also strongly on the type of flow. For bounded cavitation flows (blade passage), stark variations in the cavitation topology are observed based on the selection of the turbulence model. Second, simulations of the bubble dynamics using the Rayleigh-Plesset equation in cryogenic bubbly flows, with and without thermal effects, clearly depict the bubble radii oscillations in a 3D inducer and yield the corresponding frequencies and time scales. The thermal effects attenuate bubble oscillations and distinct dominant frequencies of oscillations are observed for different initial bubble radii. Suggestions are provided to account for the turbulence-cavitation interaction by using additional source terms in turbulence modelling equations.

1 INTRODUCTION

In Liquid Rocket Propulsion Systems (LRPS), liquid propellants in the low-pressure storage tanks are delivered to the high-pressure combustion chamber by turbopumps [1]. These turbopumps precisely control the injection pressure and flow rate to the combustion chamber and thus are classified as critical components. Design and analysis of turbopumps involve enormous complexities as they have strict high performance and weight requirements while having to balance high rotational speeds, potentially dangerous vibrations and flow instabilities [2].

Owing to stringent mass and weight constraints, the turbopumps have high rotational speeds ($\geq$ 20000 rpm) to deliver the required propellant mass flow rate to the combustion chamber. This causes cavitation at the suction side of the impeller as the static pressure of the liquid falls to its vapour pressure [1], [3]. Cavitation causes vibrations, reduction in pump efficiency, mixing losses, erratic mass flow rate, insufficient fluid power [3], and flow instabilities [4] which lead to sub-synchronous rotating cavitation [5]. An axial impeller, *inducer*, is placed in front of the main impeller on the same shaft in the turbopump assembly. The inducer raises the liquid static pressure marginally such that cavitation is avoided or reduced at the main impeller inlet. By design, inducers operate at controlled cavitating conditions to improve pumping performance [1].

Cavitation characteristics should be assessed in the early design phases. Experimental methods are the most accurate and reliable means of obtaining cavitation characteristics such as size, onset, and topology. Investigations of cryogenic and non-cryogenic cavitating flows in inducers have been carried out by Stripling and Acosta [6], Cervone *et al* [7][8], Torre *et al* [9], D'Agostino *et al* [10], Tsujimoto et al [11], and Kikuta *et al* [12]. Experiments have the greatest fidelity but they are inherently iterative, time consuming, and expensive. Numerical modelling of cavitating inducers complements the experiments and is faster, inexpensive and very useful at the early turbopump design phase. However, they lack the accurate predictive capability which the experiments provide. There are large uncertainties associated with the numerical simulations of cryogenic cavitating flows, especially on turbulence modelling and cavitation dynamics in the presence of thermal effects. Notable works on cavitation simulations

with similar characteristics to turbopump flow regimes have been carried out by Utturkar *et al* [13], Deshpande *et al* [14], Hosangadi *et al* [15] , Coutier-Delgosha *et al* [5][16], and Goncalves *et al* [17][18]. In the present work, we study two complementary aspects of turbopump simulations: the influence of turbulence modelling in simple flows relevant to turbopumps and the dynamic behaviour of bubbles in cavitating cryogenic inducer flows.

Turbulent cavitating flows can be simulated in three ways: (a) Direct Numerical Simulation (DNS), which directly solves the conservation equations of mass, momentum and energy at all relevant scales of the turbulent/cavitating flow, without any modelling; (b) Large Eddy Simulation (LES) which resolves the large scales of turbulent motion and models the small scale motion; (c) Reynolds Averaged Navier-Stokes Simulation (RANS) which solves the mean motion and models the fluctuating turbulent motion. Owing to the high rotation speeds involved, thereby high Reynolds numbers (6-22 $\times$ 10^6), DNS and LES become impractical in an industrial context [19][20][21]. RANS modelling, on the other hand, is computationally advantageous, effectively captures the dominant physical features of unsteady cavitation [22], and thus is suitable for turbopump cavitating flow applications.

Turbulence plays an important role in the prediction of phase-distribution in cavitating flows [23][24]. Cavitation bubble dynamics, especially the fluctuations in bubble sizes under variable pressure environment, also affect the flow turbulence [25][26]. Numerical prediction of cavitation bubble dynamics is done by solving the Rayleigh-Plesset equation[27]. In cryogenic cavitating flows, where the liquid-vapour density ratio is low and the point of operation is close to their critical point, thermal effects play a major role in altering the bubble dynamics [8][3]. Thermal effects correspond to the substantial depression in temperature in the vicinity of the liquid-vapour interface which is responsible for the drop in vapour pressure. Works on cavitation bubble dynamics with thermal effects include: Alhelfi *et al* [28], Alehossein *et al* [29] and Lertnuwat *et al* [30].

To the knowledge of the authors, and after a wide literature survey, no non-confidential work has specifically addressed the uncertainty associated with the choice of turbulence models on cavitation predictions in multiple flow regimes found in cryogenic turbopump inducers in a clean and systematic manner. Similarly, the numerical predictions of cavitation bubble dynamics in cryogenic inducer flows has not yet been reported thoroughly. Thus, the objectives of this work are: (1) To address the uncertainty associated with the choice of turbulence models in turbopump inducer cavitating flow simulations; (2) to quantify and analyse the characteristics of bubble dynamics in an actual turbopump inducer, such as time and length scales of bubble oscillations; (3) to transpose the knowledge gained to turbopump designers in order to assist them in their choice of modelling assumptions. In the following sections, descriptions of abstracted test cases are presented, sensitivities of turbulence closure models are analysed, cavitation bubble dynamics are numerically characterised by solving the Rayleigh-Plesset equation in real inducer flows, and finally some concluding remarks are made based on the information gained from the analyses.

2 TURBULENCE MODELLING

This work focuses on RANS simulations of cavitating flows in simplified geometries that correspond to flow regimes in an inducer. RANS-based, two-equation turbulence closure models such as $k-\omega$ SST, $k-\omega$, $k-\varepsilon$, RNG $k-\varepsilon$ are used for simulations along with the seven-equation Reynolds Stress Model [19]. Full 3D Simulations of inducers are expensive and uninformative because of multiple mutually coupled flow interactions and instabilities. These are far too complex to be addressed together, there is a lack of detailed experimental data and computational cost associated to such simulations are high. Thus, the corresponding cavitating domains in inducers are decomposed into canonical cavitating flow problems. This helps in isolating the effects of turbulence closure models, improves computational feasibility, and aides in quantifying the effects with reduced uncertainty. The following section highlights the description of numerical methods and abstracted cases.

2.1 Computational modeling

2.1.1 Numerical tools

The simulations are carried out using OpenFoam v2.2 [31], an open source CFD software. Two separate cavitation solvers were used in order to comparatively quantify the sensitivity of the choice of cavitation model. The cavitation solvers solve the conservative form of the Navier-Stokes equation but use different approaches in handling the state equation and the two-phase modelling. The first solver is based on a barotropic equation of state (denoted herein as BES - Barotropic Equation-of-state based Solver), which directly couples the density to the pressure [32][18]. The minimal speed of sound of the mixture is used as a fitting parameter for the model.

$$\psi = \frac{1}{a^2} \tag{1}$$

$$\rho_m = (1-\gamma)\rho_l + (\gamma\psi_v + (1-\gamma)\psi_l)p_s + \psi_m(p-p_s) \tag{2}$$

$$\psi_m = \gamma\psi_v + (1-\gamma)\psi_l \tag{3}$$

Here, ρ, p, ψ, a, and γ denote density, pressure, compressibility, speed of sound, and void fraction respectively. The subscripts m, v, l, and s denote mixture, vapour, liquid, and saturation quantities. The second solver is based on an additional transport equation for the liquid volume fraction α_l (TES - Transport Equation based Solver). The density of the mixture is reconstructed using the volume fraction and the respective liquid and vapour phase densities.

$$\frac{\partial \alpha_l}{\partial t} + \frac{\partial}{\partial x_j}(\alpha_l u_i) = \dot{m}^+ + \dot{m}^- \tag{4}$$

$$\rho_m = \alpha_l\rho_l + (1-\alpha_l)\rho_v \tag{5}$$

The transport equations contain source ($\dot{m}^+$) and sink ($\dot{m}^-$) terms to account for cavitation production and destruction;

cavitation source terms are modelled based on the formulae proposed by Kunz *et al* [33]. The TES is applicable for two incompressible, isothermal immiscible fluids with phase change that incorporates the Volume of Fluid (VoF) phase fraction based interface capturing methods. This solver allows for the modelling of the impact of inertial forces on cavities such as elongation, detachment, and drift of bubbles [34].

2.1.2 Test cases and boundary conditions

The cavitating flow regimes in the inducer are simplified and divided into three different sub-problems: bluff-body cavitation, attached leading edge cavitation with a pressure gradient, and internal blade passage cavitation. Fig. 1 illustrates the locations of the investigated cavitating regimes in an inducer.

The first case, simplified as an axisymmetric hemispherical headform, deals with a bluff body cavitation occurring at the inducer nose. Rouse *et al* [35] experimentally investigated cavitation in a hemispherical headform. The second case deals with the attached leading edge cryogenic cavitation using liquid hydrogen at 20 K past an axisymmetric hydrofoil with a positive pressure gradient downstream of the flow [36]. The thermal effects occurring in cryogenic fluids have not been included in the cavitation models although they affect the critical cavitation number in turbopump assemblies [37]. The third case deals with internal blade passage cavitation in inducers which is abstracted as a 2D Venturi [18].

Baseline configurations are established for the aforementioned cases with a fixed set of simulation parameters (listed in Table 1) and the effect of RANS-based turbulence models on cavitation predictions are investigated by varying the turbulence models alone. The cavitation parameters used for comparison are length, onset point, and minimum coefficient of pressure $C_{p,min}$. In the descriptions of baseline configurations, solid boundaries such as the headform, hydrofoil, and the Venturi tube are treated as no-slip walls with standard wall functions being applied. Standard wall functions correspond to law of the wall, in which the near wall velocity has a logarithmic variation in the normal direction [37]. The hemispherical headform and hydrofoil domains are designed as a wedge plane to emulate a 2D axisymmetric domain and the Venturi is configured as a 2D domain. The inflow boundary conditions prescribed the density, temperature, and velocity, of the pure liquid phase; the pressure is fixed at the outflow boundaries at the freestream value.

2.2 Grid convergence

Fully structured and optimised meshes were used for all cases. To ensure grid independence of results, a convergence analysis is carried out. Tab 1. lists the total grid points and non-dimensional first cell distance y^+ for all cases. For the sake of brevity, only the analysis pertaining to the hydrofoil case is presented here.

The time averaged density fields for coarse, nominal, and fine meshes are illustrated in Fig. 2. This represents the cavitation topology. The nominal mesh has 5.52E5 grid points in total with applied cell size grading which results in higher fidelity at the no-slip walls. The coarse and fine meshes have half and twice the number of grid points respectively in each direction while having the same cell size grading ratio. Quantities such as normalized pressure distribution (C_p) along the surface of the hydrofoil and wall normal velocity, pressure and turbulence intensity profiles are analysed to assure convergence. The invariance of integral cavitation length to grid refinement is ensured and that is set as the basis for the selection of the appropriate grid.

Table 1. Baseline simulation parameters

Parameters	H. Headform	Hydrofoil	2D Venturi
Fluid	Water	LH2	R-114
Temperature, T_∞ [K]	298	20	293
Cav. Number, σ	0.5	0.35	0.55
Velocity, U_∞ [m/s]	19.8	53.0	14.4
Pressure, p_∞ [Pa]	101325	84329	265300
Density, ρ_l [$\mathrm{kg/m^3}$]	997.05	73.47	1470.6
Turbulence model	$k-\omega$ SST	$k-\omega$ SST	$k-\omega$ SST
Mesh resolution, y_w^+	87.5	692	38.5
Grid points	5.03E5	5.52E5	6.51E5

2.3 Influence of turbulence models

Reynolds averaging of the Navier-Stokes equations yields an additional term known as the Reynolds Stress term [19]. This term requires closure and that is achieved by using a set of additional transport equations. The Boussinesq hypothesis is used to simplify the Reynolds stress tensor and expresses it as a sum of isotropic and anisotropic parts [19]. The former contains the turbulence kinetic energy k and the latter contains energy dissipation rate ε. RANS-based turbulence closure models, whose influence are under investigation, are the two-equation models such as $k-\omega$ SST, $k-\omega$, $k-\varepsilon$, Re-Normalisation Group (RNG) $k-\varepsilon$, and the seven-equation Launder-Reece-Rodi Reynolds Stress Model (RSM). The two-equation models have a transport equation for k and ε or the specific dissipation rate ω. RSM has individual transport equations for the six components of the Reynolds Stress term as well as one for ε. The intricate details of the models are left out for the sake of brevity.

In the present analysis, the baseline simulation parameters (see Tab. 1) are preserved and only the turbulence models are changed. Their effect on cavitation predictions are quantified and analysed.

2.3.1 Hemispherical headform

The simulations of bluff body cavitation is pursued using both the Barotropic Equation based Solver (BES) and Transport Equation based Solver (TES). For validation, normalized pressure (C_p) distributions along the non-dimensionalised surface distance (s/d) are obtained and compared with the experimental results of Rouse *et al* [35]. Plotted in Fig. 3 is the quantity $C_p = (p - p_\infty) \,/\, \left(0.5\rho_l U_\infty^2\right)$ along the surface distance normalized by the diameter of the hemispherical headform s/d. Here p and p_∞ are the local and freestream pressures, respectively. The minimum C_p for BES and TES

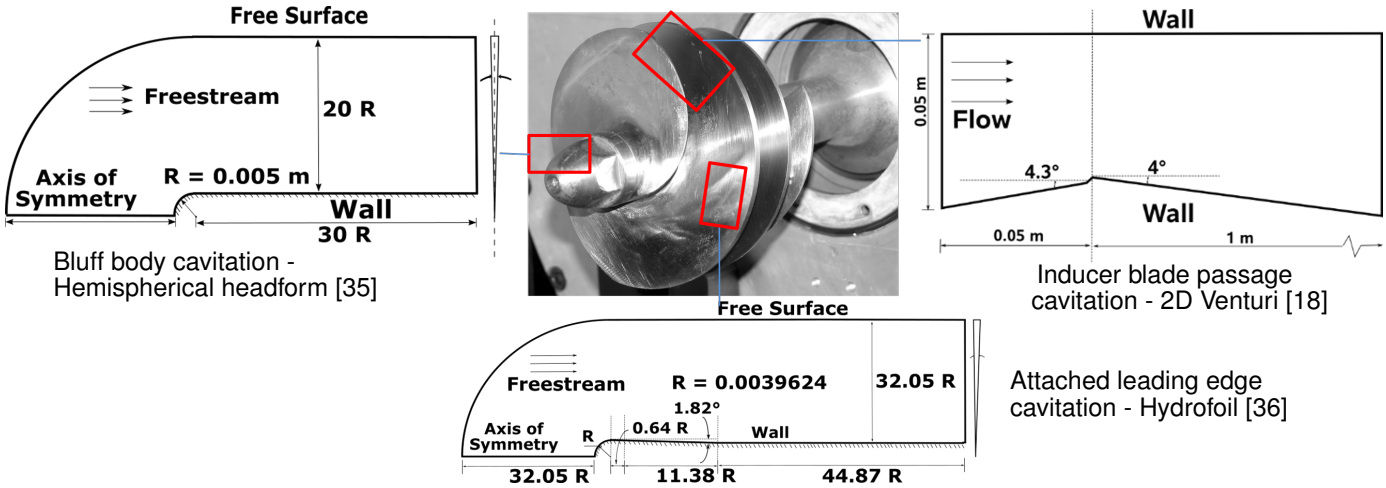

Figure 1: Simplification of a 3D inducer geometry into canonical flow problems: (top left) bluff body cavitation at the inducer boss - hemispherical headform [35], (top right) attached leading edge cavitation - hydrofoil [36], (bottom) inducer blade passage cavitation - 2D Venturi [18]

are 6.33% lower and 0.588% higher than the literature value ($C_{p,min} = -\sigma = -0.5$) respectively and the attached cavitation length (calculated at the wall) obtained for BES and TES are $0.45d$ and $0.38d$ respectively.

As the turbulence models are varied, the cavitation parameters such as $C_{p,min}$, cavitation lengths, and the distributions for pressure, density (for BES) and liquid volume fraction α_l (for TES) are quantified and compared. Fig. 4 shows the C_p distributions for various turbulence models. In BES simulations, the $k-\varepsilon$ model pressure distribution differs significantly from that of the baseline $k-\omega$ SST. A discontinuous cavity bubble is observed. The density distributions are significantly different for each model but the global cavitation

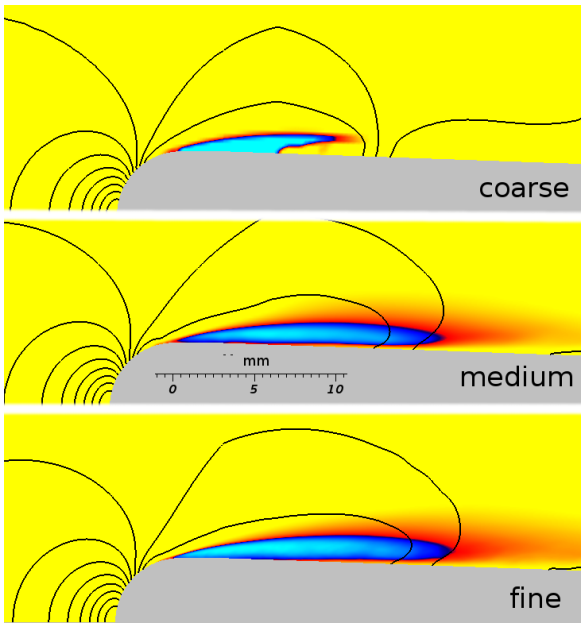

Figure 2: Grid convergence study of a hydrofoil

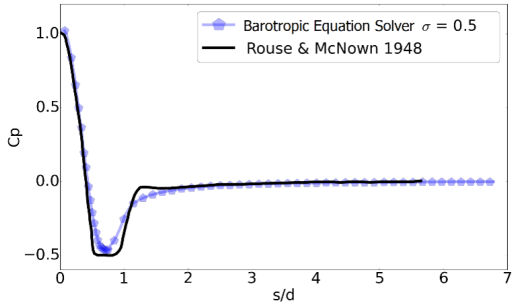

(a) BES

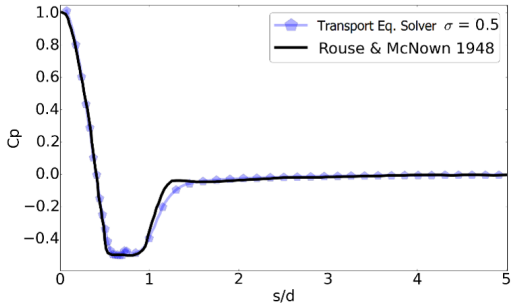

(b) TES

Figure 3: Baseline validation for BES and TES of the hemispherical headform.

length variation is minor except for RSM and $k-\varepsilon$. The RSM model predicts early cavitation onset and collapse with a 27% reduction in cavitation length. In TES simulations, all turbulence models exhibit similar pressure distributions with maximum deviation being 0.59%. Cavitation bubble size variation is negligible. This indicates that the choice of the solver has a major effect on the turbulence model influence. Tab. 2

lists the cavitation lengths, onset distances, and $C_{p,min}$ for selected turbulence models which have significant variations.

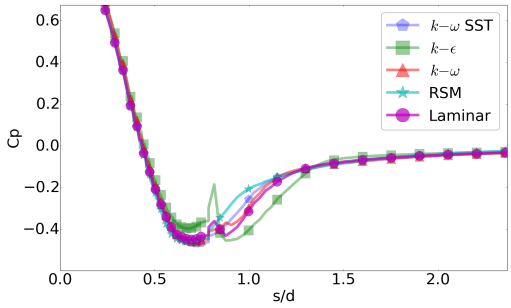

(a) Normalized pressure distribution - BES

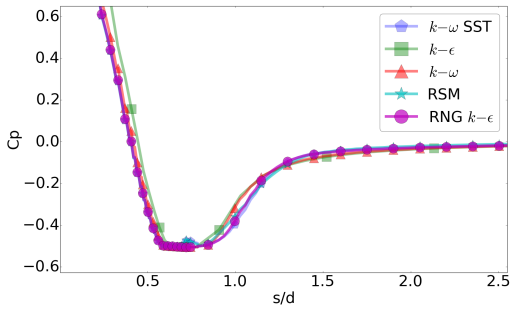

(b) Normalized pressure distribution - TES

Figure 4: Hemispherical headform normalized pressure distributions - turbulence model influence

Table 2. Hemispherical headform variations in cavitation lengths, onset distances, and $C_{p,min}$ for BES and TES - turbulence model influence.

Case	Length (d)	Onset (d)	$C_{p,min}$
SST (BES)	0.450	0.637	-0.468
SST (TES)	0.378	0.588	-0.503
Case	Δ Length (d)	Δ Onset (d)	$\Delta C_{p,min}$
		BES	
$k-\epsilon$	0.130 (28.88%)	0.021 (3.30%)	0.014 (-2.99%)
RSM	-0.124 (-27.55%)	-0.087 (-13.65%)	0.007 (-1.49%)
		TES	
$k-\epsilon$	0.028 (7.40%)	0.036 (6.12%)	-0.003 (0.59%)
$k-\omega$	0.049 (12.96%)	0.011 (1.87%)	-0.002 (0.39%)

2.3.2 *Hydrofoil*

Attached leading edge cryogenic cavitation is analysed by simulating a liquid Hydrogen flow past a hydrofoil with a positive pressure gradient downstream of the flow. The variation in the pressure coefficient, C_p, for both solvers is shown in Fig. 5. The transport-based cavitation model shows a negligible variation in $C_{p,min}$, however, the difference in the cavitation length associated with BES is $\sim 0.9d$ larger than that of TES.

In BES simulations, the pressure distributions vary by a large margin, especially for the $k-\omega$ model. It is conjectured that the positive pressure gradient downstream of the hydrofoil forces an early pressure recovery by the $k-\omega$ model due to its sensitivity to adverse pressure gradients (positive or negative) in the flow. The laminar simulation results in a similar pressure recovery, although not as strong. This is expected given the higher sensitivity (due to inflectional instability of the mean flow profile) of the laminar profile to the adverse pressure gradients. The density distributions associated with $k-\omega$ and laminar formulation also show significant differences compared to the baseline. However, the overall cavitation length variation is minor. In TES simulations, the pressure distribution patterns for all turbulence models are similar with very small differences. The liquid volume fraction distributions predicted by the turbulence models show moderate variations.

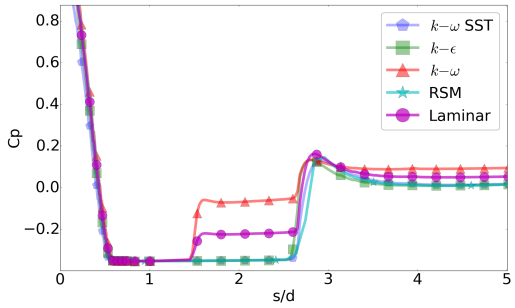

(a) Normalized pressure distribution - BES

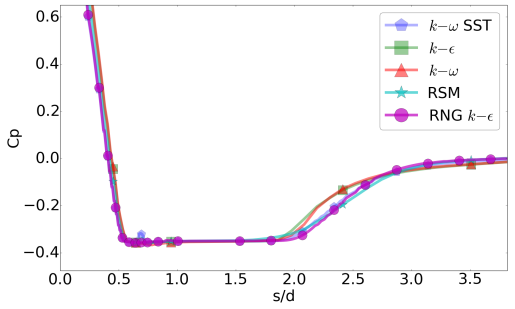

(b) Normalized pressure distribution - TES

Figure 5: Hydrofoil normalized pressure distributions - turbulence model influence

2.3.3 *2D Venturi*

The baseline case is setup for TES simulations and most initial parameters are replicated from [18]. Oscillations of the attached cavitation bubble are observed during experiments. However, in the simulations the bubble oscillations are not clearly visible. The primary cause is that the two-equation RANS models tend to over-predict the turbulent viscosity μ_t near the wall which leads to the prevention of the formation of re-entrant jet [32] and thus leading to stable cavities. Reboud

[38] proposed an empirical correction term to limit the eddy viscosity, which was not implemented in the present work.

The cavitation length obtained during the baseline simulation is 77.37 mm which lies in the range of 75-80 mm observed during experiments [18], see Tab. 3. The change in turbulence models produced drastic difference in cavitation length and topology (Fig. 6). The quantity plotted is the instantaneous α_l at a single step. The $k-\epsilon$ model yields a cavitation length which is 41% larger than that of the $k-\omega$ SST model. The $k-\omega$ however yields 15% less. Although, both $k-\omega$ and $k-\epsilon$ have similar liquid volume fraction distribution profiles with respect to the $k-\omega$ SST case.

Table 3. 2D Venturi cavity lengths and their variation for various turbulence models.

Case	Length	Δ Length
$k-\omega$ SST	0.077387 m	-
$k-\epsilon$	0.109136 m	0.031749 m (41.03%)
$k-\omega$	0.065481 m	-0.011906 m (-15.38%)
RSM	0.458370 m	0.380983 m (492.31%)
RNG $k-\epsilon$	0.490118 m	0.412731 m (533.33%)

The RSM and RNG $k-\varepsilon$ models yield very high cavitation lengths (increase of 492% and 533% respectively). The RSM behaviour is due to the high sensitivity of the modelled pressure-strain term to the adverse pressure gradients caused by the reflection of pressure from the closely placed walls. Reflection of pressure affects the redistribution of turbulent kinetic energy. The increase of TKE leads to an increase in the magnitude of the wall reflection term which in turn leads to an increase in shear stress parallel to the wall. This elongates the cavity. The slow part of the pressure-strain term is affected by the increase in velocity of the liquid phase caused by the restriction in flow, thus leading to further pressure drop and increased stretching of the vapour bubble.

The RNG $k-\varepsilon$ model differs from standard $k-\varepsilon$ formulation by using rigorous realizability constraint [39]. A noticeable difference is the usage of differential turbulent viscosity and a different model constant $C^*_{\varepsilon 2}$ which is lower in magnitude compared to the standard $k-\varepsilon$ constant $C_{\varepsilon 2}$ [19][39]. This leads to the decrease in production rate of k and dissipation rate ε. This effect reduces the value of μ_t and thereby leads to larger and more unstable cavities.

The laminar simulation does not yield an attached cavitation bubble like the rest of the models. It results in small bubbles generated at the wedge. The distribution of liquid volume fraction in the wall normal direction at three different locations (0.014 m, 0.024 m, 0.048 m) are shown in Figs. 6b, 6c, and 6d. The variation in the α distribution along the wall normal direction is significant among the turbulence models. The closest result to the corresponding literature [18] is yielded by the $k-\omega$ SST model. This analysis proves that the choice of the turbulence model carries very high importance when numerically simulating inducer flows.

3 CAVITATION DYNAMICS

Inducers, by design, operate at controlled cavitating conditions to improve overall pumping performance of the cryogenic turbopumps [1]. However, cavitation is inherently unsteady and thus a study of its dynamics shall assist in the prediction of growth and collapse of the cavity within the turbopump. In section 2, the focus is on the turbulence modelling influence on cavitation predictions. In this section, the focus is on the characterisation of cavitation bubble dynamics in real inducer flows and assessment of their potential influence on flow turbulence.

Cavitation bubble dynamics pertains to the behaviour of cavitation bubbles in a variable pressure field. As the cavitation bubbles migrate through the inducer, the changing pressure field results in a growth or collapse of the cavity. The dynamics of this behaviour is of interest in the present section. The bubble dynamics can modelled by the one-dimensional Rayleigh-Plesset equation [29]:

$$\overbrace{\frac{p_V(T_\infty)-p_\infty(t)}{\rho_l}}^{\text{Instantaneous tension}}+\overbrace{\frac{p_g}{\rho_l}\left(\frac{T_B}{T_\infty}\right)\left(\frac{R_o}{R}\right)^3}^{\text{Non-condensable gas}}+\overbrace{\Sigma\frac{dR}{dt}\sqrt{t}}^{\text{Thermal effects}}=\underbrace{R\frac{d^2R}{dt^2}+\frac{3}{2}\left(\frac{dR}{dt}\right)^2}_{\text{Inertial}}+\underbrace{\frac{4\nu_l}{R}\frac{dR}{dt}}_{\text{Viscous}}+\underbrace{\frac{2S}{R\rho_l}}_{\text{Surface tension}} \quad (6)$$

The term p_V, p_∞(t), and p_g are vapour, freestream, and gas pressures respectively; T_B is the bubble temperature, Σ is the thermal effects coefficient, R(t) is the radius of the bubble, ν_l is the kinematic viscosity of the liquid, ρ_l is the density of the liquid, and S is the surface tension of the bubble. From the Rayleigh-Plesset equation, we can find the bubble radius R(t).

As the pressure falls, the bubble grows in size until it reaches its maximum size at the lowest pressure. When the pressure recovers, the bubble starts to collapse. However, this is not a always a linear process. Oscillatory bubble may be observed and a specific frequency (and time-scale) is associated with such an oscillation.

Thermal effects play a major role in altering the bubble dynamics [15]. Thermal effects in cryogenic fluids correspond to the substantial depression in temperature in the vicinity of the liquid-vapour interface compared to freestream temperature. Cryogenic fluids in liquid rocket engines are usually close to their critical point and at these temperatures, the liquid-vapour density ratio is low. Owing to this, more liquid mass has to evaporate to sustain the cavity as the latent heat of vapourisation is drawn from the bulk liquid. Thus, the thermal effects suppress cavitation and lower the cavity pressure.

The thermal effects coefficient or the thermodynamic parameter is defined using eq. (7) [3],

$$\Sigma=\left[\frac{\lambda_{vap}^2}{T_\infty c_p\sqrt{\mathcal{A}_l}}\right]\left[\frac{\rho_v}{\rho_l}\right]^2 \quad (7)$$

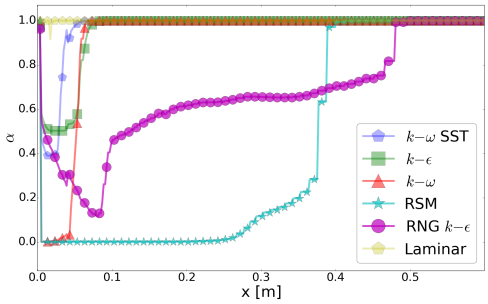

(a) α vs x

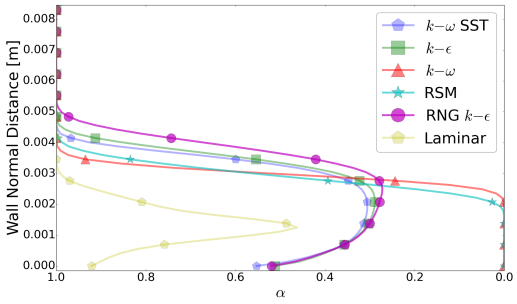

(b) Station 1 : x = 0.014 m

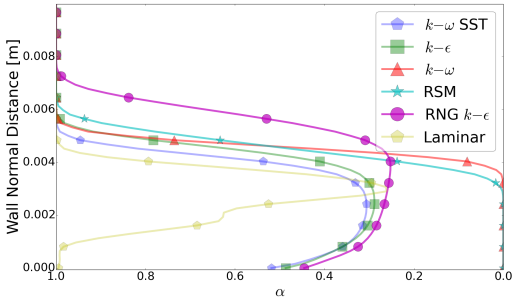

(c) Station 2 : x = 0.024 m

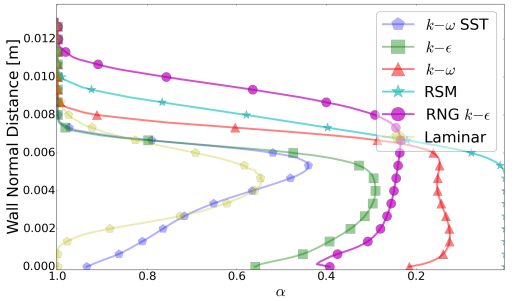

(d) Station 3 : x = 0.048 m

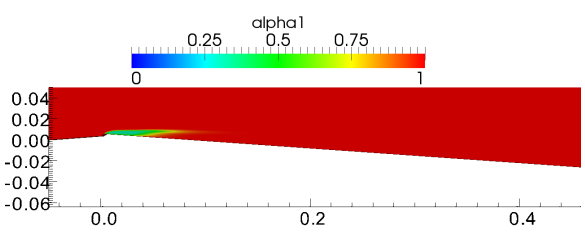

(e) $k-\omega$ SST

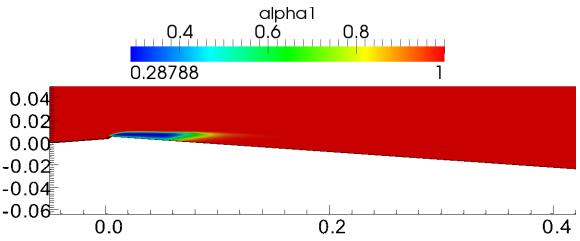

(f) $k-\epsilon$

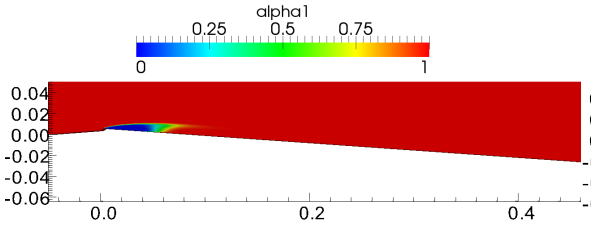

(g) $k-\omega$

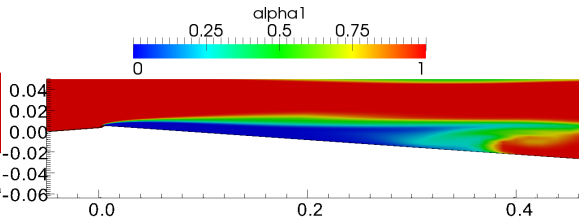

(h) RSM

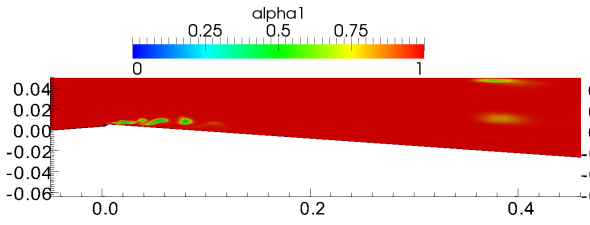

(i) Laminar

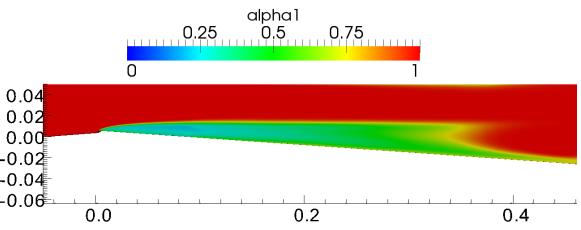

(j) RNG $k-\epsilon$

Figure 6: 2D Venturi liquid volume fraction α vs distance x distribution, wall normal α distribution, and contours for $k-\omega$ SST, $k-\epsilon$, $k-\omega$, RSM, and RNG-$k-\epsilon$ models. Laminar simulation is also presented.

Here, λ_{vap} is the latent heat of vapourisation of the liquid, c_p is the specific heat capacity of the liquid, $\mathcal{A}$ is the thermal diffusivity. Accuracy in thermal effects modelling can be improved by employing an iteration technique for the thermodynamic parameter that is expounded in [8]. The bubble growth and collapse times are severely affected by the thermodynamic parameter [3].
The present section first studies the bubble dynamics of an abstracted circumstantially-averaged pressure profile. Thereafter, the dynamics of a bubble following the individual streamtraces extracted from a three-dimensional simulation of a typical turbopump inducer is studied. Finally, a discussion on turbulence-cavitation interaction is presented.

3.1 3D Inducer

Three-dimensional incompressible flow simulations of a canonical cryogenic turbopump inducer are carried out using DLR THETA code, a pressure based extension of the in-house DLR TAU code. The inducer has a diameter in the order of 10 cm with two blade passages. Since the focus is on the bubble dynamics, no cavitation is used for the simulation. The fluid used is liquid oxygen at an ambient pressure in the order of 2-4 bar and inlet velocity in the order of 5-7 m/s. The rotation speed is in the order of 19,000-21,000 rpm. A grid convergence study was conducted which showed convergence on the circumstantially averaged pressure profile through the inducer.

3.2 Numerical implementation of R-P equation

A Python code was developed for the numerical simulation of the Rayleigh-Plesset equation for bubble dynamics (as expressed in equation (6)). The free-stream pressure (p_∞) is a time-dependant input parameter while the temperature (T_∞), density (ρ), vapour pressure (p_v), surface tension (S), latent heat (λ_{vap}), thermal conductivity (k), specific heat (c_p), thermal diffusivity ($\mathcal{A}$), and total simulation time (t) are maintained constant. The total simulation time corresponds to the convection time of the bubble in the inducer. The expression for initial non-condensable gas pressure is given by

$$p_{go} = p_\infty(0) - p_v(T_\infty) + 2S/R_o \tag{8}$$

Time is explicitly advanced using a second-order Runge-Kutta method. An initial time step value is supplied but due to the numerical instability issues that arise from a constant time stepping scheme, a variable time stepping scheme is employed. The method implemented is similar to the one in [29].

3.3 Rayleigh-Plesset in inducer mean flow

An axi-symmetrically averaged mean pressure profile in the inducer flow is obtained from the numerical simulation. This simplified pressure profile is used to study the dynamics of a bubble convected at the bulk velocity of the flow over this profile. This is done in order to simplify the analysis and qualitatively understand the bubble behaviour under a certain pressure field which is reflective of an inducer pressure field. The analysis includes 50 bubbles with increasing initial radii (R_o) from 0.01 mm to 0.5 mm (in 0.01 mm increments) passing through the mean pressure field. A set of simulation parameters are initialised and are listed in Tab. 4. The pressure profile is illustrated in Fig. 7. The analysed quantity is the radius ratio R/R_o which corresponds to the bubble length scale.

Table 4. Parameters for the numerical simulation of the Rayleigh Plesset equation

Parameters	**Value**
Fluid	Liquid Oxygen
Temperature, T_∞	80 [K]
Inlet Pressure, P_∞	3×10^5 [Pa]
Vapour Pressure, $P_v(T_\infty)$	30123 [Pa]
Liquid density, ρ_l	1190.5 [kg/m^3]
Vapour Density, ρ_v	1.4684 [kg/m^3]
Surface Tension, S	0.1522 [N/m]
Latent Heat (Vap), L	2.223×10^5 [J/kg]
Thermal Conductivity, k	0.16551 [W/m]
Specific Heat (liq.), $c_{p,l}$	1680.7 [J/kg-K]
Thermal diffusivity, $\mathcal{A}_l$	8.328×10^{-8} [m^2/s]
Initial time step, dt	2×10^{-7} [s]
Domain length, x	0.1 [m]

Fig. 7 illustrates the change in bubble sizes over time when they pass through the mean pressure field. One could clearly observe that the thermal effects inhibit the growth of bubbles and dampen the oscillations. The maximum size achieved in the presence of thermal effects is significantly smaller than the one achieved in their absence. With the increase in the initial radius, there is an increasing trend in the maximum R/R_o value. However, the maximum R/R_o value has a decreasing trend after a critical value of the initial radius.

3.4 Rayleigh-Plesset in 3D inducer flow

Since the bubbles dynamics are governed by the local pressure field (and not the mean flow pressure simulated in the section 3.3), a more physically accurate representation of the cavitation dynamics in undertaken in this section. Streamlines are randomly extracted upstream of the inducer. An individual bubble travels along the streamline from the inlet, through the rotating inducer, and onto the outlet within a particular time frame. The axial starting locations of the streamlines are fixed to a 2D plane that is 2 diameters upstream of the inducer and the radial locations are randomly selected. For these individual streamlines, pressure distribution, three-component velocity, time, and location are obtained. Then, the characteristics of bubble dynamics are quantified and analysed by solving the Rayleigh-Plesset equation with the above extracted information as input. The results do not vary when the number of streamlines are increased since we assured statistical convergence of our sample size and we neglect hydrodynamic interactions between bubbles.

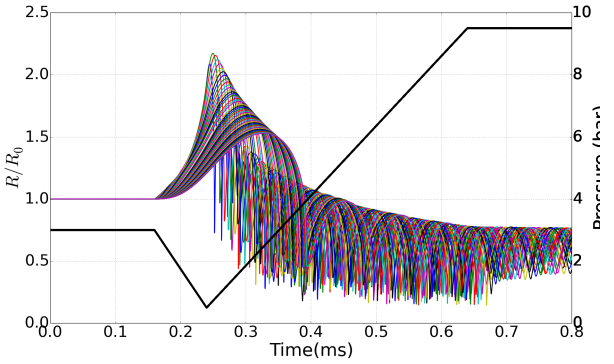

(a) No thermal effects

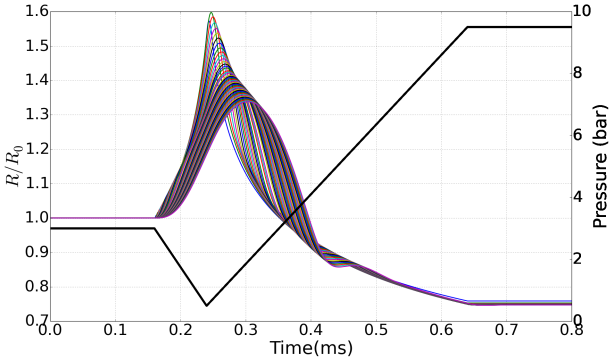

(b) Thermal effects

Figure 7: Bubble radii evolution in the presence and absence of thermal effects

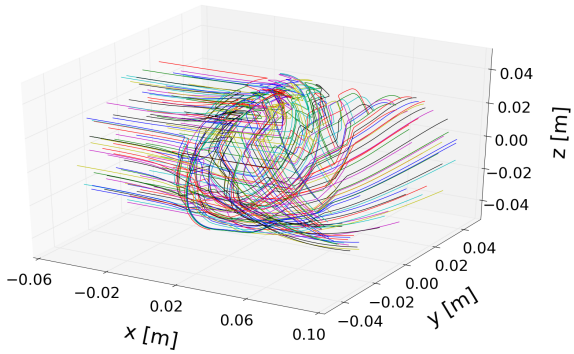

(a) Streamlines

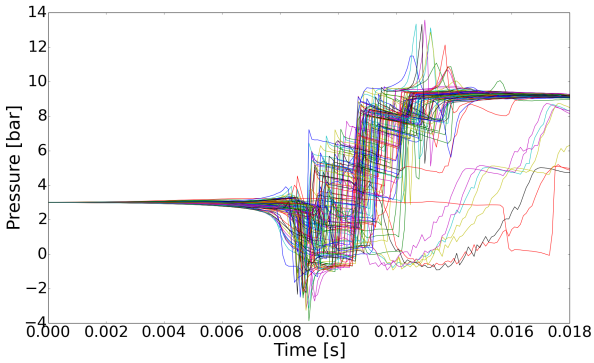

(b) Pressure Profiles

Figure 8: Extracted streamlines and corresponding pressure profiles in 3D inducer

The initial bubble radii under consideration are 10 μm, 100 μm, 150 μm, 250 μm, and 400 μm. The RP simulations without the thermal effects are pursued for all radii under consideration. The thermal effects are implemented for the 10 μm and 250 μm cases. The simulation parameters are listed in Tab. 4. The bubble streamlines and the pressure profiles are shown in Fig. 8. One could clearly observe the streamlines passing through the rotating inducer and then through the blade passages.

Applying the Rayleigh-Plesset equation, the radii evolution for each pressure profile for the corresponding initial radius is obtained. Then, a Fourier transform is applied over each of them to obtain the amplitude and the frequency of oscillations. Figs. 9 and 10 show the radii evolution plot for 10 μm amd 250 μm cases.

The evolution of the radii is represented using the ratio, R/R_o, where R and R_o are the instantaneous and initial bubble radii respectively. From Figs. 9 and 10 it is observed that the maximum radius ratio, $R/R_o|_{max}$, for 10 μm is an order of magnitude higher than that of 250 μm. Also, the thermal effects significantly reduce maximum bubble size as well as the the oscillations of the bubbles. The observed trend, from 10 μm to 400 μm, is that the maximum R/R_o drops and the bubble oscillations increase. The thermal effects reduce the amplitude of oscillations by an order of magnitude and dampen the oscillations significantly. High amplitudes of oscillation were observed in 1000-3000 Hz frequency range for the 10μm cases and in 3500-8000 Hz frequency range for the 250 μm cases.

The information regarding bubble sizes, dominant frequencies, and the time scales of oscillation are important to analyse the turbulence cavitation interaction. These time and length scales are relatable to the turbulent time and length scales. Thus, to capture the effect of bubble dynamics on turbulence production and dissipation, these physical scales should be used in RANS models.

3.5 Turbulence-cavitation interaction

Turbulence influences the phase-distribution and predictions of momentum exchange between the phases [40] and the unsteadiness associated with cavitation [38]. Velocity fluctuations in flows directly affect the production of turbulent kinetic energy in the flow. Considering a liquid flow with the presence of bubbles, where the liquid is the carrier phase and the bubbles are the dispersed phase, the some of the sources of velocity fluctuations in the carrier phase are:

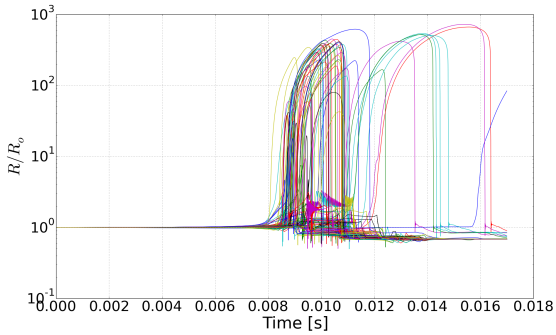

(a) No thermal effects

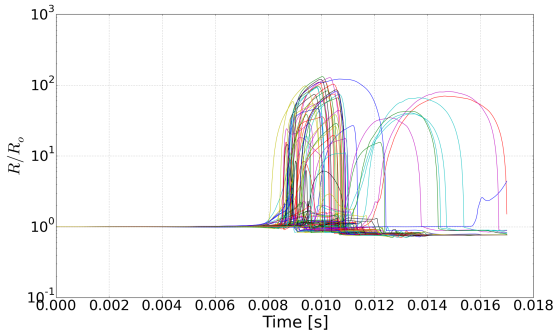

(b) With thermal effects

Figure 9: Radii evolution for 10 μm R_o case in a flow through the inducer

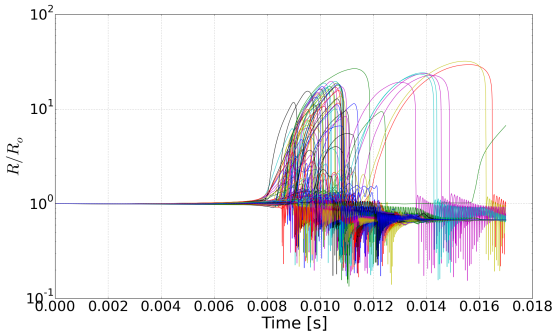

(a) No thermal effects

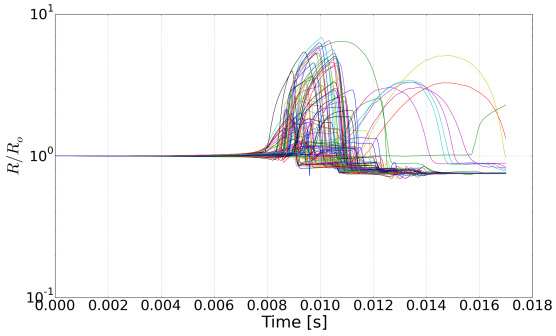

(b) With thermal effects

Figure 10: Radii evolution for 250 μm R_o case in a flow through the inducer

- Single phase/ shear induced turbulence: The fluctuations that result from an existing energy cascade fed by mean velocity gradients in the flow.
- Bubble oscillations & perturbations (pseudo-turbulence): Induced turbulence on the liquid phase near the liquid-bubble interface due to the relative motion of the bubble and oscillation of the bubble size.
- Bubble drag: Small scale fluctuations arise when the bubbles experience a drag force. The work performed by drag force is equal to the energy dissipation in the wake.

When the size of the bubbles are larger than the Kolmogorov length scale, the carrier phase turbulence is affected by the presence of bubbles and their oscillations [24]. Depending on the flow conditions, the presence of bubbles could augment or attenuate the carrier phase turbulence. However, these oscillations do not directly contribute to turbulent fluctuations but rather indirectly as pseudo-turbulent fluctuations [24][41][23]. The experimental results of Michiyoshi et al [23] show that the increase in void fraction is accompanied by an increase in velocity gradients (consequently the wall shear stress) and thus enhances turbulence production. The turbulence intensities are also augmented by the increase in gas content in the flow, although it is not always the case as observed in Serizawa et al [41].

Michiyoshi et al [23] also conjectured that the enhancement in turbulence might also be related to the increase of high frequency oscillations of the bubble. However, the turbulence properties strongly depend upon the properties of the liquid-vapour interface. In ducted flows, the overall enhancement of turbulence production is influenced by the wall generated turbulence, which is similar to that of single-phase flows. The bubble-induced turbulence is similar to the turbulence production in buoyancy driven flows.
The state-of-the-art techniques to include the interaction effects in RANS-models consist of addition of source terms to the corresponding equations of turbulent kinetic energy (k), dissipation rate (ε), and specific dissipation rate (ω) in the case of two-equation models. For Reynolds stress model, an interfacial work term, which acts as a source/sink of turbulence energy, is added to the stress transport equation and the pressure-strain correlation is modified to include the bubble dynamics effects [42][24]. The default time scale used in the two-equation models is the turbulence time scale $\tau = k/\varepsilon$. To include the effects of bubble dynamics, the bubble oscillation time scale (reciprocal of the oscillation frequency) is substituted for τ [26].

4 Conclusion

Numerical modelling of cavitating cryogenic inducers are a necessary complement to experimental campaigns and

are very useful in the early turbopump design stages. Simulations using RANS turbulence closure models provide detailed flow field characteristics, are computationally affordable, and can be integrated into optimization tools for rapid design convergence. At the same time, the uncertainty related to the flow modelling must be understood and quantified. This work highlights the non-negligible effect of the selection of the turbulence model on characteristic flow setups relevant to cryogenic turbopump inducers.

The variation among the turbulence models is the greatest for cavitation solvers that directly couple the density and the pressure (barotropic models); transport equation solvers show far less variation among the turbulence models. The variability of cavitation predictions among the turbulence models also depends on the type of flow under consideration. In bounded flow problems, as occurring in blade passage cavitation in cryogenic turbopumps, the cavitation predictions by different RANS-based turbulence models vary drastically. This large uncertainty may lead to drastic variations in the predicted pump efficiency and for other important design parameters. The study of the bubble dynamics shows the importance of the thermal effect in damping out the oscillatory growth of the cavities. For non-thermosensitive cavitation, the pressure recovery results in a high-frequency growth and shrinking of the cavity size. When the modelled thermal effects are included, the bubble oscillation is almost completely suppressed. The study of the dynamics permits a characterization of the time-scales of the cavities. This could be used as a means to improve the turbulence-cavitation coupling for turbulence modelling.

Inclusion of source terms in turbulence models to account for multiphase interactions, and problem specific corrections to account for rotation flow anisotropies and flow unsteadiness can lead to an improvement in predictive capabilities of numerical simulations. Accurate predictive capabilities are desired and in many cases required to save development costs. These extensions to classical should be considered as further research.

ACKNOWLEDGMENT

This work was carried out at the DLR Institute of Aerodynamics and Flow Technology, Göttingen, Germany in collaboration with Delft University of Technology, the Netherlands. The authors would like to thank Dr. Klaus Hannemann, head of the Spacecraft Department in DLR and Dr. Eberhard Gill, the head of Space Systems Engineering in TU Delft.

REFERENCES

[1] Sutton, G. & Bilbarz, O. (2010) Rocket Propulsion Elements 7th Edition. *Wiley*.

[2] Wu, Y., Li, S., Liu, S., Dou, H.S. & Qian, Z. (2013) Vibration of hydraulic machinery. *Springer*.

[3] Brennen, C.E. (2013) Cavitation and bubble dynamics. *Cambridge University Press*.

[4] Pace, G., Valentini, D., Pasini, A., Torre, L., Fu, Y. & d'Agostino, L. (2015) Geometry effects on flow instabilities of different three-bladed inducers. *ASME J. Fluids Eng.* **137**(4), 041304.

[5] Coutier-Delgosha, O., Caignaert, G., Bois, G. & Leroux, J. (2012) Influence of the blade number on inducer cavitating behavior. *ASME J. Fluid Eng.* **134**, 081304–1–11.

[6] Stripling, L. & Acosta, A. (1962) Cavitation in turbopumps - part 1. *ASME J. Fluids Eng.* **84**(3), 326–338.

[7] Cervone, A., Torre, L., Pasini, A. & d'Agostino, L. (2009) Cavitation and turbopump hydrodynamics research at alta spa and pisa university. In Fluid Machinery and Fluid Mechanics, Springer, pp. 80–88.

[8] Cervone, A., Testa, R., Bramanti, C., Rapposelli, E. & D'Agostino, L. (2005) Thermal effects on cavitation instabilities in helical inducers. *J. Propul. Power* **21**(5), 893–899.

[9] Torre, L., Cervone, A., Pasini, A. & d'Agostino, L. (2011) Experimental characterization of thermal cavitation effects on space rocket axial inducers. *ASME J. Fluids Eng.* **133**(11), 111303.

[10] d'Agostino, L. (2013) Turbomachinery developments and cavitation. *VKI Lecture Series on Fluid Dynamics Associated to Launcher Developments, von Karman Institute of Fluid Dynamics, Rhode-Saint-Genese, Belgium, Apr* pp. 15–17.

[11] Tsujimoto, Y., Yoshida, Y., Maekawa, Y., Watanabe, S. & Hashimoto, T. (1997) Observations of oscillating cavitation of an inducer. *ASME J. Fluids Eng.* **119**(4), 775–781.

[12] Kikuta, K., Yoshida, Y., Watanabe, M., Hashimoto, T., Nagaura, K. & Ohira, K. (2008) Thermodynamic effect on cavitation performances and cavitation instabilities in an inducer. *ASME J. Fluids Eng.* **130**(11), 111302.

[13] Utturkar, Y., Wu, J., Wang, G. & Shyy, W. (2005) Recent progress in modeling of cryogenic cavitation for liquid rocket propulsion. *Prog. Aerosp. Sci* **41**(7), 558–608.

[14] Deshpande, M., Feng, J. & Merkle, C.L. (1997) Numerical modeling of the thermodynamic effects of cavitation. *ASME J. Fluids Eng.* **119**(2), 420–427.

[15] Hosangadi, A. & Ahuja, V. (2005) Numerical study of cavitation in cryogenic fluids. *ASME J. Fluids Eng.* **127**(2), 267–281.

[16] Coutier-Delgosha, O., Morel, P., Fortes-Patella, R. & Reboud, J.L. (2005) Numerical simulation of turbopump inducer cavitating behavior. *Int. J. Rotating Mach.* **2005**(2), 135–142.

[17] Goncalvès, E. & Patella, R.F. (2010) Numerical study of cavitating flows with thermodynamic effect. *Comput. Fluids* **39**(1), 99–113.

[18] Goncalves, E. (2014) Modeling for non isothermal cavitation using 4-equation models. *Int. J. Heat Mass Transfer* **76**, 247–262.

[19] Pope, S.B. (2000) Turbulent flows. *Cambridge university press*.

[20] Payri, R., Tormos, B., Gimeno, J. & Bracho, G. (2010) The potential of large eddy simulation (les) code for the modeling of flow in diesel injectors. *Math. Comput. Modell.* **52**(7), 1151–1160.

[21] Ahuja, V., Hosangadi, A. & Arunajatesan, S. (2001) Simulations of cavitating flows using hybrid unstructured meshes. *ASME J. Fluids Eng.* **123**(2), 331–340.

[22] Wang, J., Wang, Y., Liu, H., Huang, H. & Jiang, L. (2015) An improved turbulence model for predicting unsteady cavitating flows in centrifugal pump. *Int. J. Numer. Meth. H.* **25**(5), 1198–1213.

[23] Michiyoshi, I. & Serizawa, A. (1986) Turbulence in two-phase bubbly flow. *Nucl. Eng. Des.* **95**, 253–267.

[24] Lathouwers, D. (1999) Modelling and simulation of turbulent bubbly flow. Ph.D. thesis, TU Delft, Delft University of Technology.

[25] Serizawa, A. & Kataoka, I. (1990) Turbulence suppression in bubbly two-phase flow. *Nucl. Eng. Des.* **122**(1), 1–16.

[26] Rzehak, R. & Krepper, E. (2013) Bubble-induced turbulence: Comparison of cfd models. *Nucl. Eng. Des.* **258**, 57–65.

[27] Prosperetti, A. (1982) A generalization of the rayleigh–plesset equation of bubble dynamics. *Phys.Fluids* **25**(3), 409–410.

[28] Alhelfi, A. & Sunden, B. (2015) Simulations of cryogenic cavitation of low temperature fluids with thermodynamics effects. *Int. J. Mech. Aerosp. Ind. Mechatron. Eng.* **9**, 8.

[29] Alehossein, H. & Qin, Z. (2007) Numerical analysis of rayleigh–plesset equation for cavitating water jets. *Int. J. Numer. Methods Eng.* **72**(7), 780–807.

[30] Lertnuwat, B., Sugiyama, K. & Matsumoto, Y. (2001) Modeling of the thermal behavior inside a bubble. In Fourth International Symposium on Cavitation. University of Tokyo.

[31] Weller, H.G., Tabor, G., Jasak, H. & Fureby, C. (1998) A tensorial approach to computational continuum mechanics using object-oriented techniques. *Comput. Phys.* **12**(6).

[32] Brennen, C.E. (2005) Fundamentals of Multiphase Flow. *Cambridge University Press*.
[33] Kunz, R.F., Boger, D.A., Stinebring, D.R., Chyczewski, T.S., Lindau, J.W., Gibeling, H.J., Venkateswaran, S. & Govindan, T. (2000) A preconditioned navier–stokes method for two-phase flows with application to cavitation prediction. *Comp. Fluids* **29**(8), 849–875.
[34] Senocak, I. & Shyy, W. (2002) A pressure-based method for turbulent cavitating flow computations. *J. Comput. Physics* **176**, 363–383.
[35] Rouse, H. & McNown, J.S. (1948) Cavitation and pressure distribution: head forms at zero angle of yaw. *Technical report*, State University of Iowa.
[36] Hord, J. (1973) Cavitation in Liquid Cryogens: Hydrofoil. II, volume 2156. National Aeronautics and Space Administration.
[37] Kim, J. & Song, S.J. (2016) Measurement of temperature effects on cavitation in a turbopump inducer. *ASME J. Fluids Eng.* **138**(1), 011304.
[38] Reboud, J., Coutier-Delgosha, O., Pouffary, B. & Fortes-Patella, R. (2003) Numerical simulation of unsteady cavitation flows: Some applications and open problems. In Fifth International Symposium on Cavitation.
[39] Yakhot, V., Orszag, S., Thangam, S., Gatski, T. & Speziale, C. (1992) Development of turbulence models for shear flows by a double expansion technique. *Phys. Fluids* **4**(7), 1510–1520.
[40] Wang, S., Lee, S., Jones, O. & Lahey, R. (1987) 3-d turbulence structure and phase distribution measurements in bubbly two-phase flows. *Int. J. Multiphase Flow* **13**(3), 327–343.
[41] Serizawa, A., Kataoka, I. & Michiyoshi, I. (1975) Turbulence structure of air-water bubbly flow-ii. local properties. *Int. J. Multiphase Flow* **2**(3), 235–246.
[42] Lance, M. & Bataille, J. (1991) Turbulence in the liquid phase of a uniform bubbly air–water flow. *J. Fluid Mech.* **222**, 95–118.